# Supplementary Information: Europium Cyclooctatetraene Nanowire Carpets: A Low-Dimensional, Organometallic, and Ferromagnetic Insulator

Felix Huttmann,[†] Nico Rothenbach,[‡] Stefan Kraus,[†] Katharina Ollefs,[‡] Lucas M. Arruda,[¶] Matthias Bernien,[¶] Danny Thonig,[§] Anna Delin,[§,∥,⊥] Jonas Fransson,[§] Kurt Kummer,[#] Nicholas B. Brookes,[#] Olle Eriksson,[§,@] Wolfgang Kuch,[¶] Thomas Michely,[†] and Heiko Wende[*,‡]

†*II. Physikalisches Institut, Universität zu Köln, Zülpicher Strasse 77, D-50937 Köln, Germany*

‡*Universität Duisburg-Essen and Center for Nanointegration Duisburg-Essen (CENIDE), Lotharstr. 1, D-47057 Duisburg, Germany*

¶*Institut für Experimentalphysik, Freie Universität Berlin, Arnimallee 14, 14195 Berlin, Germany*

§*Department of Physics and Astronomy, Materials Theory, Uppsala University, SE-75120 Uppsala, Sweden*

∥*Department of Applied Physics, School of Engineering Sciences, KTH Royal Institute of Technology, Electrum 229, SE-16440 Kista, Sweden*

⊥*SeRC (Swedish e-Science Research Center), KTH Royal Institute of Technology, SE-10044 Stockholm, Sweden*

#*European Synchrotron Radiation Facility, 71 Avenue des Martyrs, CS40220, F-38043 Grenoble Cedex 9, France*

@*School of Science and Technology, Örebro University, SE-701 82 Örebro, Sweden*

E-mail: heiko.wende@uni-due.de

## Sum-rule analysis

As mentioned in the corresponding section of the main text, applying sum rules to the rare-earth Eu $M_{5,4}$ absorption edges is challenging. We want to emphasize especially the following points:

(i) The XAS show up to 70 eV higher photon energy than the $M_4$ edge very small but non-negligible signals, which could be assigned to $M_{5,4}$ contributions. Therefore, it is not clear where to cut off the integration, which effects both, the values of $m_L$ and $m_S$.

(ii) The XMCD exhibits a nonzero contribution between the $M_5$ and $M_4$ edges, by which the separation of the edges is complicated, but important for the exact determination of the spin magnetic moment. Fig. S. 1 illustrates these two points. It shows also the averaged XAS and normalized XMCD spectra [see Fig. 2 of the main text] and displays additionally on the right axis how $\mu_L$ and $\mu_S$ change depending on where the cut-off of the $M_4$ absorption edge is chosen. Furthermore, we indicate exemplarily three different energies (vertical dotted lines) where one might separate the $M_5$ and $M_4$ absorption edges, which affects the magnetic spin moment significantly. The shown energy

dependency of the magnetic moments displays the range by which their value can vary and therefore reflects the total error bars given by the uncertainties of the separation of the two edges.

(iii) Moreover it is known, that the relative errors of the sum rule analysis for the heavy 3*d*-metals is already up to 10 % and 20 % for orbital and spin magnetic moment, respectively, and increasing with the atomic number.[1–3] Hence, we estimate the total errors for our sum rule analysis to be up to $0.3\,\mu_B$ for $m_L$ and $0.6\,\mu_B$ for $m_S$. Consequently, we want to point out that the interpretation of our sum-rule analysis can also allow a small but finite value of the orbital magnetic moment which can originate e.g. from a non-integer valence state of Eu.

Furthermore, we note that the presented sum rule analysis is not considering that the evaluated values of $\mu_L$ and $\mu_S$ are calculated from the spectra measured at grazing incidence, and therefore do not take the projection of the moments along the X-ray beam into account. However, we expect that for the isotropic $4f^7$ shell such corrections are negligible, and assume that the applied field of 9 T is sufficient to align the magnetic moment into the direction of the photon *k*-vector. This is also confirmed by the fact that the sum rule analysis for normal incidence (not shown here) results in the same magnetic moments as for grazing incidence.

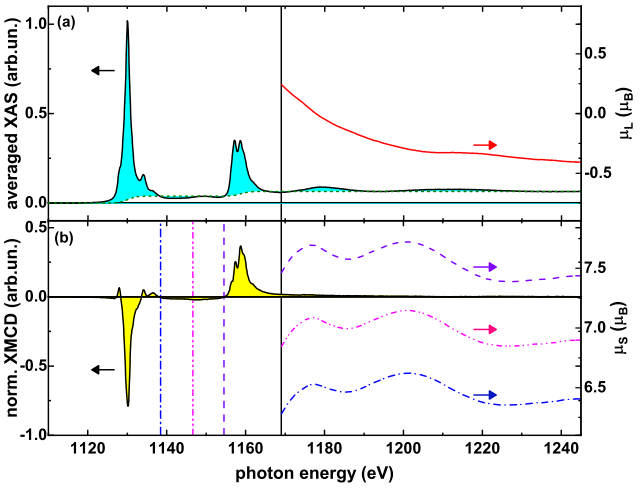


Fig. S. 1: (a) Polarization-averaged XAS $\frac{1}{2}(\mu^+ + \mu^-)$ (black solid line) of the Eu $M_5$ and $M_4$ edges measured at grazing incidence with $\theta = 60°$, 5 K, 9 T, and with left ($\mu^-$) and right ($\mu^+$) circularly polarized X-rays. The spectra are presented on a vertical scale that has been adjusted to zero in the pre-edge region and to one at the peak maximum of the averaged XAS (see main text). Also indicated is a step function (green dashed line) used to separate the $M_{5,4}$ contributions (blue area) from the continuum. The right *y* axis displays the magnetic orbital moment depending on the cut-off after the $M_4$ edge (red solid line), which we obtain by sum rule analysis. (b) Normalized XMCD ($\mu^+ - \mu^-$) (black solid line and yellow area). The right *y* axis displays the magnetic spin moment depending on the cut-off after the $M_4$ edge for exemplary three different energies (vertical dotted lines at 1138.4 eV, 1146.6 eV and 1154.5 eV) separating the absorption edges.

## Temperature dependence

Fig. S. 2 shows the averaged XAS and normalized XMCD spectra for 0.6 ML EuCot on Gr/Ir(111) measured with an external magnetic field of $B = 9\,\mathrm{T}$ in grazing incidence at a sample temperature of $T = 5\,\mathrm{K}$ (black), $T = 7\,\mathrm{K}$ (red), and $T = 10\,\mathrm{K}$ (blue). The spectral shape shows only a weak dependence on the temperature but changes in the XMCD peak height due to the increased spin fluctuations with increasing temperature are seen. Within the error bar the magnetic orbital moment stays constant close to zero, i.e. $\mu_L = (-0.1 \pm 0.3)\,\mu_B$. With increased temperature, the magnetization decreases by 9 % and 10 %, respectively, as compared to the value at 5 K. We attribute the reduction in magnetization to increased spin fluctuations with increasing temperature.

## Radiation damage

In the XAS and XMCD measurements shown in Fig. 2 (main text) we carefully avoided radiation damage by tuning the flux of the X-rays and the illuminated area on the sample. To get insight into the potential effect of radiation damage on our molecular system, we additionally took spectra after intentionally in-

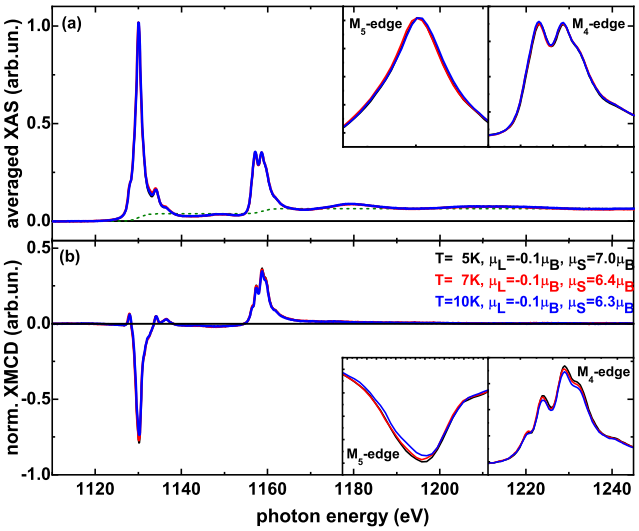


Fig. S. 2: Polarization-averaged XAS (a) and normalized XMCD (b) for 0.6 ML EuCot on Gr/Ir(111) measured with an external magnetic field of $B = 9\,\mathrm{T}$ in grazing incidence at a sample temperature of $T = 5\,\mathrm{K}$ (black), $T = 7\,\mathrm{K}$ (red) and $T = 10\,\mathrm{K}$ (blue).

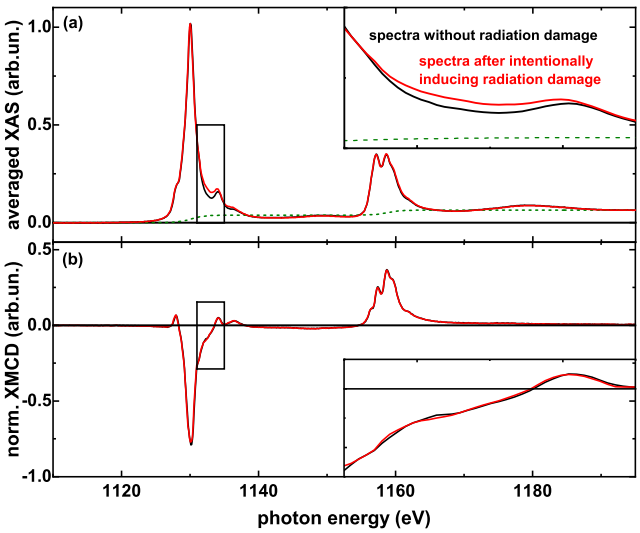


Fig. S. 3: Polarization-averaged XAS (a) and normalized XMCD (b) for 0.6 ML EuCot on Gr/Ir(111) measured with an external magnetic field of $B = 9\,\mathrm{T}$ in grazing incidence at a sample temperature of $T = 5\,\mathrm{K}$. The effect of radiation damage is displayed by comparison of the spectra without damage (black solid line) and with intentionally induced damage (red solid line).

ducing radiation damage by increasing the flux of the X-rays. Fig. S. 3 displays how radiation damage changes the absorption spectra. By increasing the X-ray flux by about an order of magnitude, the synchrotron radiation damages the molecular system slightly, which results in small changes of the fine structure of the XAS $M_5$ edge but leaving the XMCD unaffected (see inset). As a consequence, the radiation damage changes the values of $m_L$ and $m_S$ by 10 % to smaller values. The displayed changes in the fine structure by the radiation are fully developed and not further increasing with additional measuring time.

Interestingly, despite the small changes in the spectral shape, the effect of the radiation damage is crucial with respect to the hysteresis and the associated magnetic ordering within the wires. The radiation damage leads to a closing of the hysteresis loop shown in Fig. 3 (main text) and therefore destroys the ferromagnetic ordering within the wires (see Fig. S. 4). The curvature of both magnetization curves is not influenced by the radiation damage. How exactly the radiation influences the structure of the wire stays unclear and has to be investigated further. But presumably the radiation or the created photoelectrons break some bonds in the cyclooctatetraene-ring and thereby destroy the indirect coupling between the Eu-ions which cannot be mediated afterwards. The lineshape of the averaged XAS displays a divalent $Eu^{2+}$ state, for both, the spectra with and without radiation damage.

## Theoretical determination of the valence stability

In order to theoretically determine the valence stability in 4f systems, one needs to calculate the total energy difference between a divalent $f^{n+1}[spd]^2$ and a trivalent $f^n[spd]^3$ configuration. Unfortunately, evaluation of this energy in conventional DFT is not possible because of the poor description of the $4f$ electron correlations within this theory. However, for localized systems wherein the Coulomb interaction is much stronger than the hybridization between $4f$ and valence electrons, one can evaluate the valence of the system using the Born-Haber cycle within the DFT approach.[4,5] The essential assumption

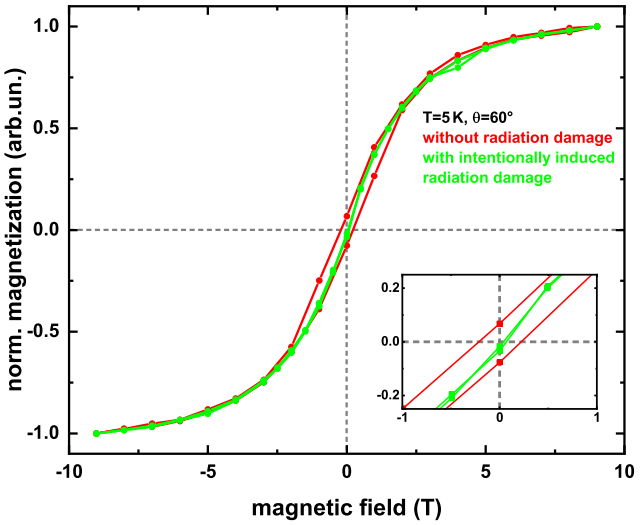


Fig. S. 4: Comparison of the field-dependent XMCD signal at the Eu $M_5$ edge for $-9 \leq B \leq 9\,\mathrm{T}$ without radiation damage (of different sample prepared in the same manner as in [Fig. 3. (b)], red curve) and after intentionally inducing damage (green curve). Both curves are normalized such that the XMCD at $B = 9\,\mathrm{T}$ has the value 1.0. Insets magnify the magnetization in the range $-1 \leq B \leq 1\,\mathrm{T}$.

in the Born-Haber cycle is that the $4f$ electrons are so localized that they behave the same in the atom and in the solid. In this respect, the expression for the energy difference between a pure divalent and a pure trivalent configuration is the following

$$E_{II-III} = (E_{tot} - E_{atom})_{II} - (E_{tot} - E_{atom})_{III} - E_{fd} - \Delta E_c \quad (1)$$

wherein $E_{tot}$ is the total energy, $E_{atom}$ is the energy of an isolated atom, $E_{fd}$ is called the promotion energy from $4f$ to $5d$ and finally $\Delta E_c$ corresponds to the atomic correction energy. The latter two values used here are taken from Ref.[4] More details about the Born-Haber cycle can be found in Refs.[4,5]

Using the expression above for the energy stability of di- and trivalent configurations, we have determined the valence stability of a bare Eu wire and a EuCot wire. The results predict that for both systems the valence configurations are divalent. The corresponding energy in equation (1) is equal to $-1.94\,\mathrm{eV}$ for a bare wire and $-2.08\,\mathrm{eV}$ for a EuCot wire. The valence energy for a bulk Eu atom has been reported to be $-0.78\,\mathrm{eV}$ in Ref.,[5] which also favors the divalent configuration. Hence, the formation of EuCot does not change the divalent configuration of the Eu atoms from their bulk values. These results are in agreement with the experimental observations made here and with previous theoretical results.[6–9] We note that a determination of valence stability using the Born-Haber cycle is unique in distinguishing metastable configurations from absolute stability, something which methods based on e.g. the LDA+U method suffer from. Furthermore, knowledge of the energy position of the $4f$ shell with respect to the Fermi level, as provided by the Born-Haber cycle, allows to estimate at which energies this channel for electron tunneling in STM experiments may open up.

The electronic structure is modelled by the full- potential linear muffin-tin orbitals (FP-LMTO) code RSPt.[10,11] Strongly correlations in the materials are treated by a combination of DFT and DMFT (DFT + DMFT). Details of this implementation have been presented elsewhere.[12–15]

## Theoretical estimates of finite temperature effects of the coercive field

In order to establish a realistic value of the nearest neighbor Heisenberg exchange, we first calculated the ordering temperature $T_C$ as a function of the nearest-neighbor exchange interaction $J$ in the absence of anisotropy (see Fig. S. 5). Note that the nearest-neighbor interaction $J$ is only along the wire; direct exchange between the wires is set to zero. From the figure we conclude that in order to obtain an ordering temperature of $T_C^{\mathrm{theo}} = 6\,\mathrm{K}$, the Heisenberg exchange interaction must be 1.2 meV. We take this as a realistic strength of the exchange of EuCot.

While in theory $T_C^{\mathrm{theo}}$ is the temperature where the phase transition from ferromagnetic

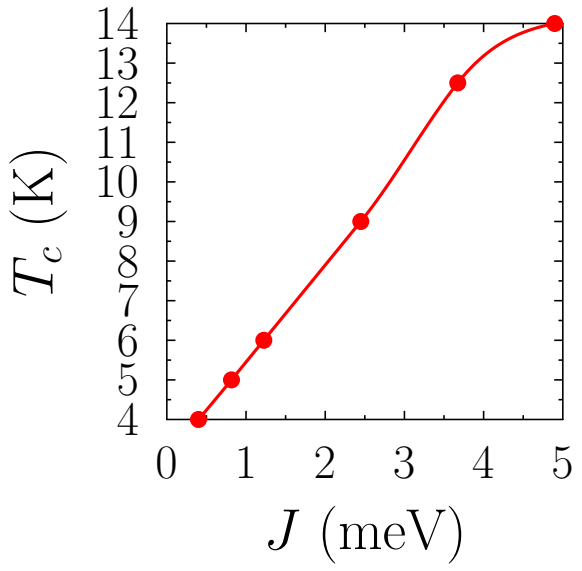


Fig. S. 5: Simulations of the ordering temperature $T_C$ as a function of exchange interactions $J$. The crystalline anisotropy $K$ is set to zero.

to paramagnetic state occurs, we have defined $T_C^{\text{exp}}$ in experiment as the temperature at which the coercive field disappears. To compare experiment and theory, we have calculated finite-temperature values of the coercive field, using Monte Carlo simulations and an effective spin Hamiltonian that contains nearest neighbor Heisenberg exchange, dipole-dipole interaction, a magnetic anisotropy term and a Zeeman energy (see equation (1), main text). Note that the nearest-neighbor interaction $J$ is only along the wire; direct exchange between the wires is set to zero. We show in Fig. S. 6 the simulated value of the coercive field with respect to the strength of the exchange interaction and the magnetocrystalline anisotropy. Note that three different temperatures were considered, 1 K, 3 K, and 5 K. It is clear that the coercive field is larger for enhanced values of the magnetocrystalline anisotropy and exchange interaction, which is to be expected. We also show in Fig. S. 7 the value of the coercive field as function of temperature, for a fixed value of $J$, i.e. 1.2 meV, and for varying values of magnetocrystalline anisotropy. We find that the coercive field decays very fast with respect to temperature. Due to noise and the discrete simulation mesh of the magnetic field in the calculation, the coercivity never goes down to exactly zero. We thus mark in Fig. S. 6 by white contour lines the values for $J$ and $K$ at which the coercive field is as low as 20 mT. We can then extract values for $J$ and $K$ that match the experiment. In experiment, the coercivity vanishes between 5 and 7 K. Values of $J$ and $K$ slightly above the white line in the topmost panel of Fig. S. 6 would thus be consistent with the experiment. For an exchange interaction $J = 1.2$ meV, the theoretical value needed to have a $T_C$ of 6 K (see Fig. S. 5), an anisotropy of more than 0.6 meV would be required, while for $J = 2.4$ meV, around 0.3 eV anisotropy would suffice.

It is well known that close to the critical temperature, but also at very low temperatures, quantum effects occur and the Boltzman distribution of the thermal bath, as it is applied in our simulations, should be modified. It is discussed in literature[16,17] that a (semi-) quantum description of the thermal bath in Monte Carlo simulations leads to a rescaled classical temperature. Hence, it can be argued that the temperature for which one should extract from Fig. S. 7 an appropriate anisotropy should be somewhat smaller than the experimental temperature of 5 K. We have therefore estimated that at 3 K a magnetic anisotropy of 0.5 meV results in a coercive field of 200 mT, which is close to the experimentally observed value.

# References

(1) Wu, R.; Wang, D.; Freeman, A. First principles investigation of the validity and range of applicability of the x-ray magnetic circular dichroism sum rule. *Phys. Rev. Lett.* **1993**, *71*, 3581.

(2) Wu, R.; Freeman, A. Limitation of the Magnetic-Circular-Dichroism Spin Sum Rule for Transition Metals and Importance of the Magnetic Dipole Term. *Phys. Rev. Lett.* **1994**, *73*, 1994.

(3) Scherz, A.; Wende, H.; Baberschke, K.; Minar, J.; Benea, D.; Ebert, H. Relation

between $L_{2,3}$ XMCD and the magnetic ground-state properties for the early 3d element V. *Phys. Rev. B* **2002**, *66*, 184401.

(4) Johansson, B. Energy position of 4f levels in rare-earth metals. *Phys. Rev. B* **1979**, *20*, 1315.

(5) Delin, A.; Fast, L.; Johansson, B.; Wills, J.; Eriksson, O. Method for Calculating Valence Stability in Lanthanide Systems. *Phys. Rev. Lett.* **1997**, *79*, 4637.

(6) Atodiresei, N.; Dederichs, P. H.; Mokrousov, Y.; Bergqvist, L.; Bihlmayer, G.; Blügel, S. Controlling the Magnetization Direction in Molecules via Their Oxidation State. *Phys. Rev. Lett.* **2008**, *100*, 117207.

(7) Zhang, X.; Ng, M.-F.; Wang, Y.; Wang, J.; Yang, S.-W. Theoretical Studies on Structural, Magnetic, and Spintronic Characteristics of Sandwiched $Eu_nCot_{n+1}$ ($n = 1-4$) Clusters. *ACS Nano* **2009**, *3*, 2515–2522.

(8) Xu, K.; Huang, J.; Lei, S.; Su, H.; Boey, F.; Li, Q.; Yang, J. Efficient organometallic spin filter based on Europium-cyclooctatetraene wire. *J. Chem. Phys.* **2009**, *131*, 104704.

(9) Yao, X.; Yuan, S.; Wang, J. Theoretical Studies of Sandwich Molecular Wires with Europium and Boratacyclooctatetraene Ligand and the Structure on a H-Ge(001)-2x1 Surface. *J. Phys. Chem. C* **2016**, *120*, 7088–7093.

(10) Wills, J.; Cooper, B. Synthesis of band and model Hamiltonian theory for hybridizing cerium systems. *Phys. Rev. B* **1987**, *36*, 3809.

(11) Wills, J.; Eriksson, O.; Alouani, M.; Price, D. *Full-Potential LMTO Total Energy and Force Calculations*; Electronic Structure and Physical Properies of Solids. Lecture Notes in Physics; Springer-Verlag Berlin Heidelberg, **1999**; Vol. 535.

(12) Marco, I.; Minár, J.; Chadov, S.; Katsnelson, M.; Ebert, H.; Lichtenstein, A. Correlation effects in the total energy, the bulk modulus, and the lattice constant of a transition metal: Combined local-density approximation and dynamical mean-field theory applied to Ni and Mn. *Phys. Rev. B* **2009**, *79*, 115111.

(13) Grechnev, A.; Marco, I.; Katsnelson, M.; Lichtenstein, A.; Wills, J.; Eriksson, O. Theory of bulk and surface quasiparticle spectra for Fe, Co, and Ni. *Phys. Rev. B* **2007**, *76*, 035107.

(14) Thunström, P.; Marco, I.; Eriksson, O. Electronic Entanglement in Late Transition Metal Oxides. *Phys. Rev. Lett.* **2012**, *109*, 186401.

(15) Grånäs, O.; Marco, I.; Thunström, P.; Nordström, L.; Eriksson, O.; Björkman, T.; Wills, J. Charge self-consistent dynamical mean-field theory based on the full-potential linear muffin-tin orbital method: Methodology and applications. *Computational Materials Science* **2012**, *55*, 295–302.

(16) Bergqvist, L.; Bergman, A. Realistic finite temperature simulations of magnetic systems using quantum statistics. *Phys. Rev. Materials* **2018**, *2*, 013802.

(17) Woo, C.; Wen, H.; Semenov, A.; Dudarev, S.; Ma, P.-W. Quantum heat bath for spin-lattice dynamics. *Phys. Rev. B* **2015**, *91*, 104306.

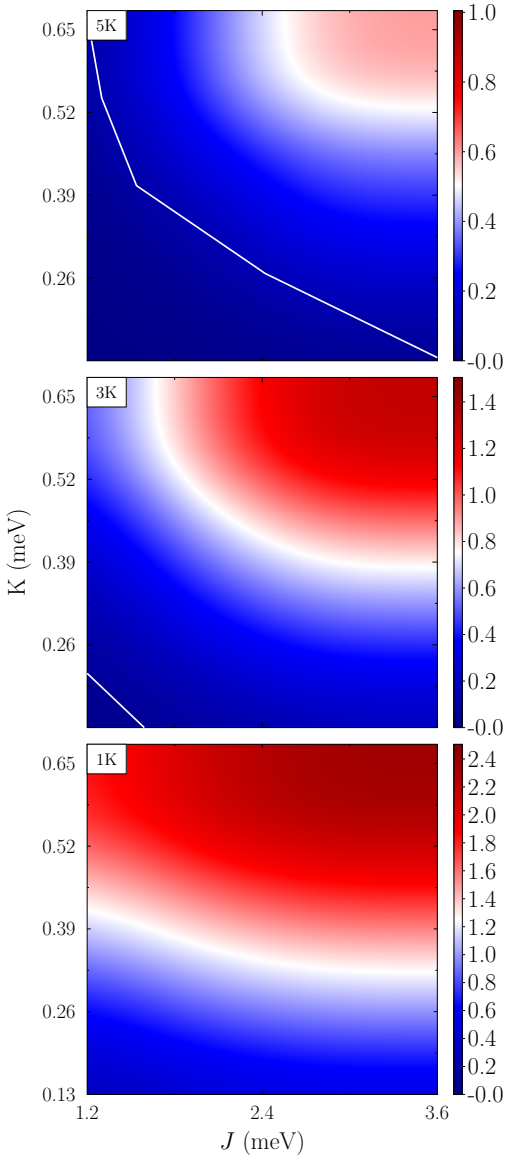


Fig. S. 6: The coercive field $B^{coer}$ in $T$, represented by the color scale, is shown as a function of the uniaxial magnetocrystalline anisotropy $K$ and the nearest-neighbor interaction $J$ for three different temperatures (different panels). The white line is the contour line where the coercive field is 20 mT. Note that the color scale is adjusted for every temperature.

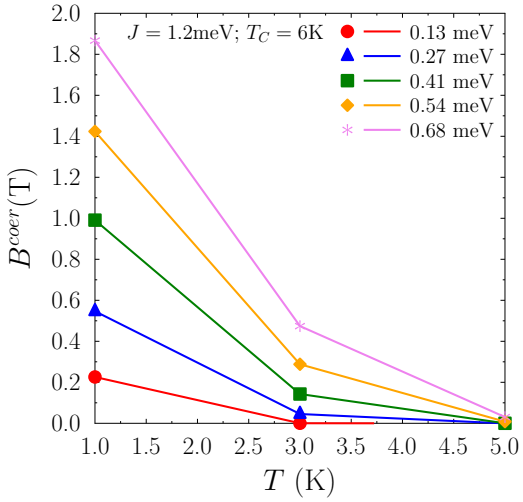


Fig. S. 7: Coercive field $B^{coer}$ as a function of temperature $T$ for different values of the uniaxial magnetocrystalline anisotropy $K$. The nearest-neighbor interaction $J$ is 1.2 meV. Lines are added to guide the eye.